SCIENTIFIC REPORTS

OPEN

3D β-Ni(OH)$_2$ nanowires/RGO composite prepared by phase transformation method for superior electrochemical performance

Wenxiu He[1], Xingsheng Li[1], Shengli An[1], Tongjun Li[2], Yongqiang Zhang[1] & Jinlong Cui[1]

In order to improve the capacity and rate performance of nickel-metal hydride (Ni-MH) batteries, we proposed a simple phase transformation method to synthesis 3D β-nickel hydroxide nanowires/reduced graphene oxide (β-Ni(OH)$_2$ NWs/RGO) composite. β-Ni(OH)$_2$ nanowires with diameters of 20–30 nm and lengths up to several micrometers were decorated on RGO layers, forming 3D network structure. The 3D β-Ni(OH)$_2$ NWs/RGO composite displayed a discharge capacity of 343.2 mAh/g at 0.2C, and the capacity values has almost no loss after 100th cycles. When the discharge rate was at 5C, the capacity reached a value of 272.7 mAh/g, and its capacity retention was 79.5%. It showed good capacity and rate performance as a positive material for Ni-MH batteries.

In recent years, the new energy electric vehicles and hybrid electric vehicles have been received great attention account of the rapid energy consumption and the environmental pollution[1,2]. However, the main factor limiting the development of new energy vehicles is energy storage systems (Ni-MH batteries, Lithium-ion batteries, supercapacitors, etc.)[3–7]. Therefore, the energy storage systems have been become a research hotspot. Ni-MH batteries are widely used in hybrid electric devices because of their high energy density, fast charging and discharging, low cost, safety, etc[8–10]. Moreover, Ni(OH)$_2$ as positive material of Ni-MH batteries is an key factor affecting the capacity performance[11]. Nevertheless, the volume change of Ni(OH)$_2$ is large in the rapid charging-discharging process, leading to the rapid capacity fade[12,13]. In order to improve the capacity performance of Ni(OH)$_2$ electrode, significant research efforts have focused on the synthesis of nanostructured Ni(OH)$_2$ with different structures, such as nanoflowers[14–17], nanoplates[18–20], nanobelts[21], nanorods[22], nanowires[23–26]. Among these structures, 1D nanostructured Ni(OH)$_2$ is considered as an ideal positive material of Ni-MH batteries among these structures, because of its large surface areas and small volume change during charging-discharging process. Therefore, the preparation Ni(OH)$_2$ nanowires with high structural stability is a hot topic for practical applications of Ni-MH batteries.

Owing to the unique physical and chemical properties of graphene, it can increase conductivity of Ni(OH)$_2$ and effectively relieve its volume expansion[27,28]. Thus, many researchers use graphene to compensate the disadvantages of Ni(OH)$_2$ as positive material of Ni-MH batteries. To date, many methods have been used to synthesize Ni(OH)$_2$/graphene compounds, such as hydrothermal method[29], template method[30], and electrochemical deposition method[31], etc. Nevertheless, α-Ni(OH)$_2$ nanowires and non-nanowires α-/β-Ni(OH)$_2$ are generally obtained by the hydrothermal approach, and the reduction process of graphene oxide to graphene needs to add reducing agent. For template method, the use of template agent and surfactant results in increased costs. The post-treatment process is complex and needs to remove the template agent. For electrochemical deposition method, it is necessary to precisely control the reaction conditions in the deposition process, such as temperature, pH value, current or voltage, etc. As a typical layered structure material, Ni(OH)$_2$ contains two main crystalline structures, α- and β-Ni(OH)$_2$[32]. β-Ni(OH)$_2$ is consisted of close-stacked 2D Ni(OH)$_2$ layers without intercalated species, and α-Ni(OH)$_2$ is consisted of close-stacked 2D Ni(OH)$_2$ layers with anions and water molecules[33]. Therefore, the theoretical specific capacity of α-Ni(OH)$_2$ is higher than that of β-Ni(OH)$_2$. However, α-Ni(OH)$_2$ is not stable in alkaline medium and easily transformed into β-Ni(OH)$_2$. 3D β-Ni(OH)$_2$ NWs/RGO

[1]School of Chemistry Chemistry and Chemical Engineering, Inner Mongolia University of Science and Technology, Baotou, 014010, China. [2]College of Physics and Material Science, Henan Normal University, Xinxiang, 453007, China. Correspondence and requests for materials should be addressed to W.H. (email: nmghwx@sina.com) or S.A. (email: shengli_an@126.com)
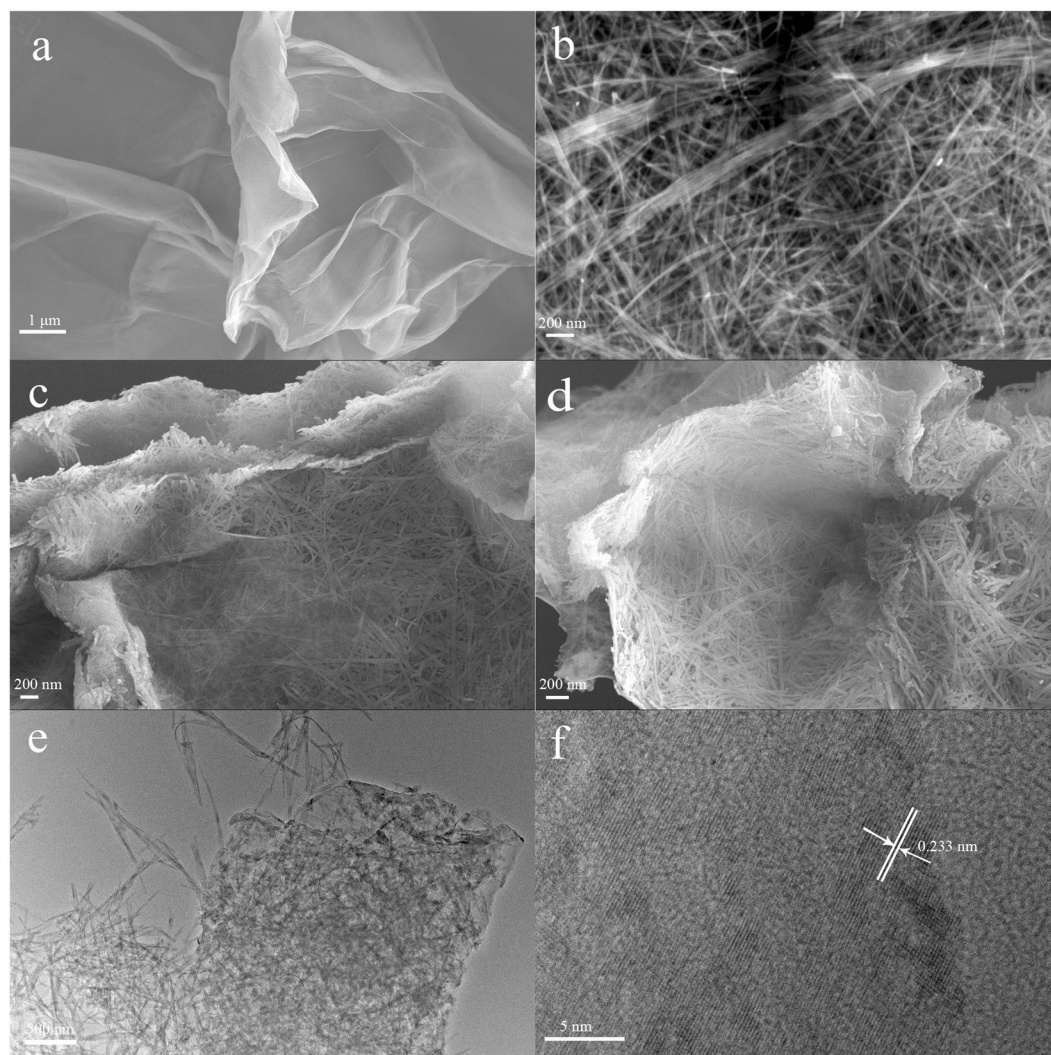
Figure 1. SEM images of GO (**a**), β-Ni(OH)$_2$ NWs (**b**), α-Ni(OH)$_2$ NWs/RGO (**c**), β-Ni(OH)$_2$ NWs/RGO (**d,e**) TEM image and (**f**) HRTEM image of β-Ni(OH)$_2$ NWs/RGO.

was synthesized by phase transformation method according to this property of Ni(OH)$_2$. The prepared method of β-Ni(OH)$_2$ NWs/RGO by phase transformation method was rarely reported previously.

The phase transformation method is quite simple due to their low cost, easy operation, safe, and environmentally friendly natures. In the phase transformation process, α-Ni(OH)$_2$ was transformed into β-Ni(OH)$_2$ at 180 °C for 30 min in a NaOH solution, and the morphology of nanowires was retained. In 3D β-Ni(OH)$_2$ NWs/RGO composite, 1D β-Ni(OH)$_2$ nanowires and 2D RGO sheets formed a stable 3D network structures that provided sufficient space and rapid transfer paths for ions and electrons[34]. The RGO sheets could enhance the conductivity of β-Ni(OH)$_2$ nanowires and effectively alleviate the volume expansion during charging-discharging process, and the β-Ni(OH)$_2$ nanowires could prevent the aggregation of the RGO sheets. Under the synergistic effects of β-Ni(OH)$_2$ NWs and RGO sheets, the 3D β-Ni(OH)$_2$ NWs/RGO composite exhibited a better electrochemical performance. β-Ni(OH)$_2$ NWs/RGO composite displayed superior rate performance compared with α-Ni(OH)$_2$ NWs/RGO and β-Ni(OH)$_2$ nanoplates/RGO (β-Ni(OH)$_2$ NPs/RGO) composites.

Results and Discussion

The morphology evolution process of α-Ni(OH)$_2$ NWs/RGO composite in NaOH solution were characterized by SEM analysis. Figure 1a shows the SEM image of GO. It can be seen that GO sheets are like transparent voile with many wrinkles. Figure 1b exhibits the typical nanowires of β-Ni(OH)$_2$, the average diameters were 20 nm. For α-Ni(OH)$_2$ NWs/RGO composite, α-Ni(OH)$_2$ nanowires with lengths up to several micrometers and diameters of about 30 nm were supported on RGO sheets to form 3D network structure in Fig. 1c. Figure 1d dispalys the morphology of β-Ni(OH)$_2$ NWs/RGO composite after being hydrothermally treated for 30 min, and its morphology was still unchanged. The change of crystal phase has taken place in NaOH solution, and the nanowires morphology was maintained[35]. Compared with the pure β-Ni(OH)$_2$ NWs, the diameter of β-Ni(OH)$_2$ NWs becomes larger for β-Ni(OH)$_2$ NWs/RGO composite, which is attributed to the addition of RGO. β-Ni(OH)$_2$ NWs were uniformly loaded on RGO sheets (Fig. 1e). The lattice space of β-Ni(OH)$_2$ NWs is 0.233 nm, which corresponds
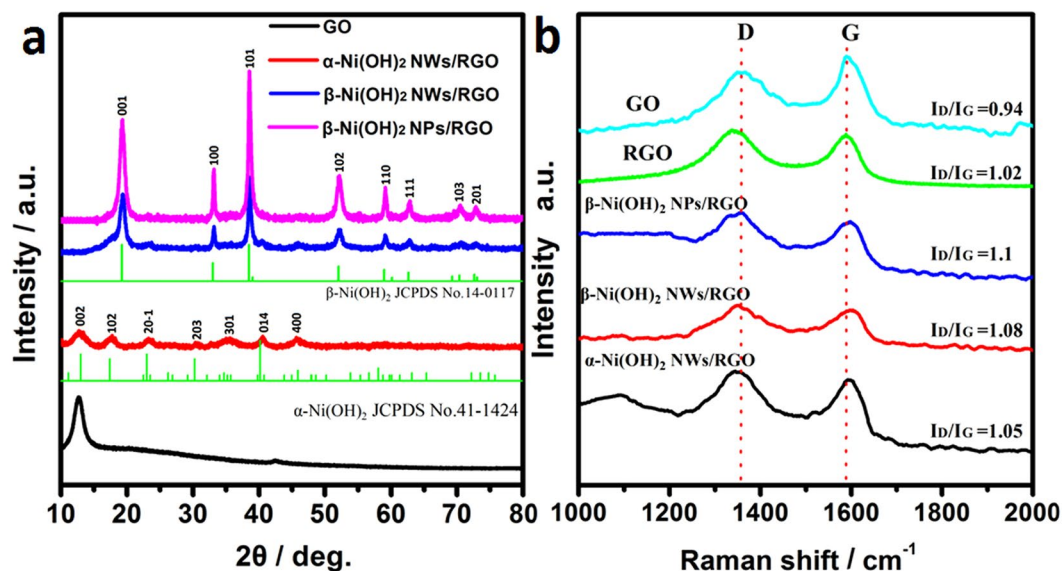
Figure 2. (**a**) XRD patterns of GO, α-Ni(OH)$_2$ NWs/RGO, β-Ni(OH)$_2$ NWs/RGO, β-Ni(OH)$_2$ NPs/RGO. (**b**) Raman spectra of GO, RGO, α-Ni(OH)$_2$ NWs/RGO and β-Ni(OH)$_2$ NWs/RGO.

to (101) plane (Fig. 1f). It further demonstrates that the prepared materials are β-Ni(OH)$_2$ NWs and RGO composites. The EDS elemental mapping image displays Ni, O and C elements, indicating that Ni(OH)$_2$ NWs are uniformly dispersed on the whole RGO sheets (Fig. S1). The EDS analysis further suggests that the synthesized material is consisted of Ni(OH)$_2$ and RGO. For β-Ni(OH)$_2$ NPs/RGO composite, nanowires were completely transformed into nanoplates (Fig. S2).

Figure 2a shows the XRD patterns of GO and Ni(OH)$_2$/RGO composites. For GO, there was a characteristic diffraction peak at $2\theta = 12.5°$, indicating the successful oxidation of the spectral pure graphite[36]. In the Ni(OH)$_2$/RGO composites, no characteristic peaks from RGO was observed in XRD patterns, which may be attributed to the ultrathin layer of RGO and strong diffraction peaks of Ni(OH)$_2$[37]. The main characteristic peaks of α-Ni(OH)$_2$ NWs/RGO are corresponded to paraotwayite-type α-Ni(OH)$_2$ (JCPDS 41-1424)[38]. After hydrothermal treated, the characteristic peaks of α-Ni(OH)$_2$ disappeared, and eventually converted to β-Ni(OH)$_2$ (JCPDS 14-0117)[39]. β-Ni(OH)$_2$ NPs/RGO had good crystallinity compared with other samples. The weight contents of Ni(OH)$_2$ in α-Ni(OH)$_2$ NWs/RGO and β-Ni(OH)$_2$ NWs/RGO are approximately 95% and 90%, respectively, as calculated from thermogravimetric analysis (TGA) curves (Fig. S3).

As the hydrothermal time increases, the phase and morphology of the Ni(OH)$_2$ also changes. In alkaline solution, the anion between the layers of α-Ni(OH)$_2$ can be removed after aging, and the α phase of the Ni(OH)$_2$ is converted into the β phase. In the absence of alkaline solution, the crystallization rate of β-Ni(OH)$_2$ is slower than the dissolution rate of α-Ni(OH)$_2$. However, in the NaOH solution, the dissolution rate of α-Ni(OH)$_2$ decreases, and the crystallization rate of β-Ni(OH)$_2$ increases[35]. Therefore, α-Ni(OH)$_2$ can be completely converted to β-Ni(OH)$_2$ at 180 °C for 30 min in an alkaline solution. After completely converting β-Ni(OH)$_2$ NWs, the morphological changes of β-Ni(OH)$_2$ are related to agglomeration and Ostwald ripening[40]. To reduce the surface energy of the crystal, Ni(OH)$_2$ nanowires are aggregated into wider nanowires after complete phase transformation. As the hydrothermal time increases, Ni(OH)$_2$ nanowires in the defective area break and form nanoplates.

To further confirm the existence and reduction degree of RGO in the composite, we use Raman spectra to characterize the sample. Figure 2b shows that these characteristic D and G peaks of these samples are located at about 1350 and 1590 cm^{-1}, respectively. The D peak is associated with first-order zone boundary phonons, indicating the presence of graphene defects. The G peak is attributed to the first-order scattering of the E$_{2g}$ vibrational mode, indicating the in-plane bond-stretching motion of the pairs of C sp^2 atoms[41]. Generally, the I_D/I_G ratio is used to determine the reduction level of RGO[42]. The values of RGO (1.02), α-Ni(OH)$_2$ NWs/RGO (1.05), β-Ni(OH)$_2$ NWs/RGO (1.08), and β-Ni(OH)$_2$ NWs/RGO (1.1) are higher than that of GO(0.94), indicating that GO is deeply reduced to form a high-level disordered structure of RGO.

XPS analysis is employed to further identify the elemental valence states of Ni(OH)$_2$/RGO samples. From survey spectrum of the α-Ni(OH)$_2$ NWs/RGO, the C 1s, O 1s, Ni 2p and S 2p peak can clearly be seen (Fig. 3a), but the S 2p peak can not be observed in β-Ni(OH)$_2$ NWs/RGO, suggesting α-Ni(OH)$_2$ NWs is transformed into β-Ni(OH)$_2$ NWs during the hydrothermal reaction in NaOH solution. The C 1s spectrum of XPS is shown in Fig. 3b. The C 1s peak of the Ni(OH)$_2$/RGO composites is divided into C=C (284.6 eV), C-C (285.2 eV), C-O/C-O-C (286.4 eV), and C=O (287.9 eV) peaks. The intensity peaks of C=C and C-C bonds in β-Ni(OH)$_2$ NWs/RGO are stronger than that of α-Ni(OH)$_2$ NWs/RGO, demonstrating that GO was further reduced during the hydrothermal reaction process[43]. The Ni 2p spectrum of XPS is shown in Fig. 3c. The spin separation energy of Ni(OH)$_2$ in α-Ni(OH)$_2$ NWs/RGO and β-Ni(OH)$_2$ NWs/RGO between Ni 2p1/2 (873.4 eV) and Ni 2p3/2 (855.8 eV) is 17.6 eV, which confirm the presence of Ni(OH)$_2$ in the composite[44]. The binding energy of
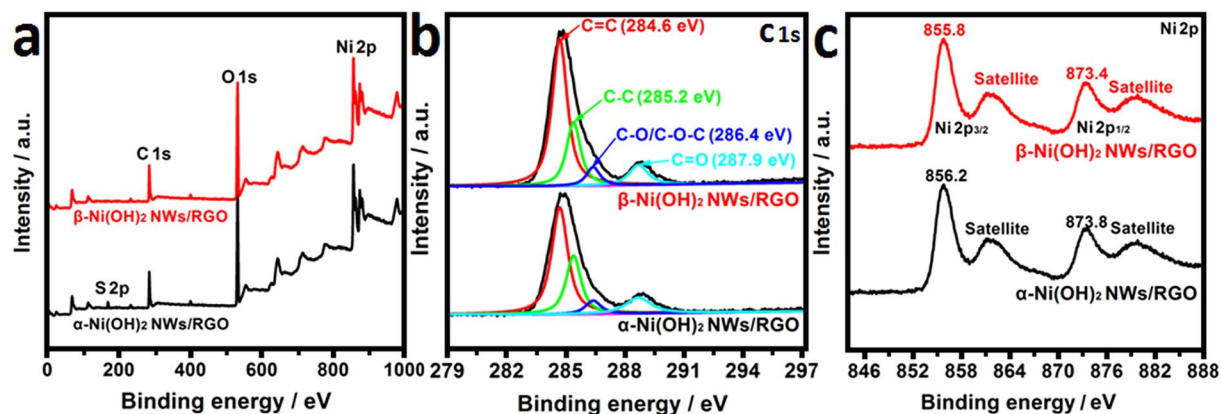
Figure 3. (**a**) XPS survey spectrum of α-Ni(OH)$_2$ NWs/RGO and β-Ni(OH)$_2$ NWs/RGO, (**b**) C1s and (**c**) Ni 2p XPS spectra of the obtained α-Ni(OH)$_2$ NWs/RGO and β-Ni(OH)$_2$ NWs/RGO.
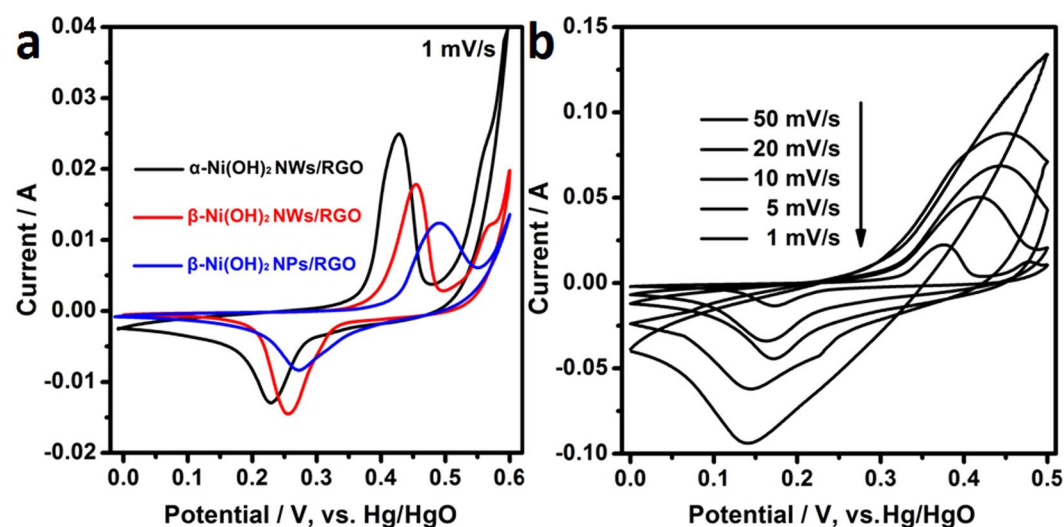
Figure 4. (**a**) CV curves of α-Ni(OH)$_2$ NWs/RGO, β-Ni(OH)$_2$ NWs/RGO, and β-Ni(OH)$_2$ NPs/RGO. Scan rate: 1 mV/s, (**b**) CV curves of β-Ni(OH)$_2$ NWs/RGO at different scan rates.

Electrode materials	E_R/V	E_O/V	$E_O - E_R$/V
α-Ni(OH)$_2$ NWs/RGO	0.229	0.426	0.197
β-Ni(OH)$_2$ NWs/RGO	0.255	0.455	0.2
β-Ni(OH)$_2$ NPs/RGO	0.272	0.491	0.219

Table 1. Electrochemical parameters from the CV curves of electrode materials.

α-Ni(OH)$_2$ NWs/RGO is higher than that of β-Ni(OH)$_2$ NWs/RGO, which is attributed to the presence of SO_4^{2-} in α-Ni(OH)$_2$ NWs.

Figure 4a displays the CV profiles of Ni(OH)$_2$-based with RGO electrodes at 1 mV/s. A couple of well-defined redox peaks is seen from the CV curves due to the conversion of nickel ions at different oxidation states. The Faradaic reactions of Ni(OH)$_2$ electrode is based on the following redox reaction: $Ni(OH)_2 + OH^- \leftrightarrow NiOOH + H_2O + e^-$[45]. The potential difference ($E_O - E_R$) between oxidation potential (E_O) and reduction potential (E_R) is used to represent the reversibility of the electrode material. In Table 1, the reversibility of α-Ni(OH)$_2$ NWs/RGO and β-Ni(OH)$_2$ NWs/RGO is better than that of β-Ni(OH)$_2$ NPs/RGO, because the $E_O - E_R$ value ranked in the order of α-Ni(OH)$_2$ NWs/RGO (0.197 V) < β-Ni(OH)$_2$ NWs/RGO (0.2 V) < β-Ni(OH)$_2$ NPs/RGO (0.264 V). This is because Ni(OH)$_2$ nanowires can provide faster transfer channels for ions and electrons compared to Ni(OH)$_2$ nanosheets. For different electrodes, with the same scan speed and active material mass, the larger the CV curve area of the electrode is, the larger the discharge capacity is. It can be concluded that the specific capacities of α-Ni(OH)$_2$ NWs/RGO and β-Ni(OH)$_2$ NWs/RGO are higher than that of β-Ni(OH)$_2$ NPs/RGO at the same test conditions.
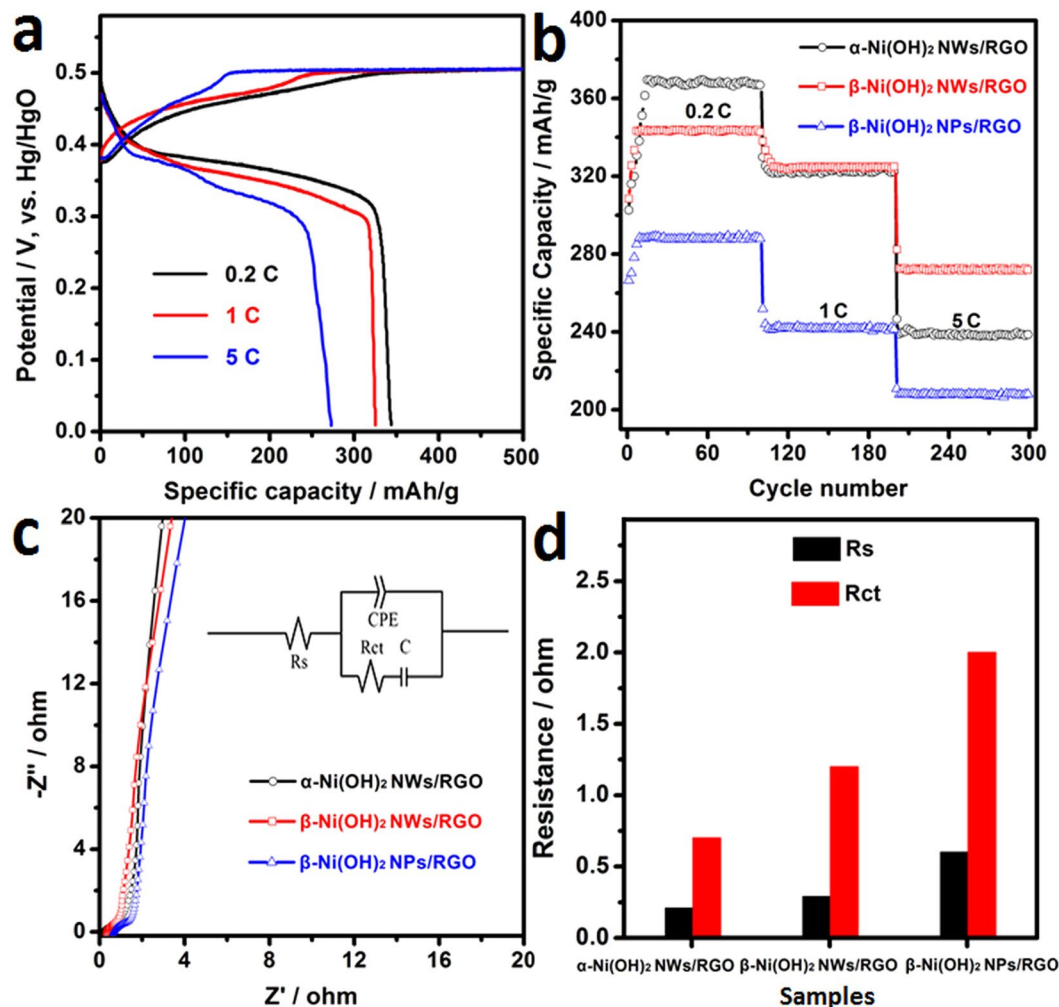
Figure 5. (**a**) Charge-discharge curves of β-Ni(OH)$_2$ NWs/RGO at different rates, (**b**) Cycling stability curves of α-Ni(OH)$_2$ NWs/RGO, β-Ni(OH)$_2$ NWs/RGO, and β-Ni(OH)$_2$ NPs/RGO, (**c**) Nyquist plots of α-Ni(OH)$_2$ NWs/RGO, β-Ni(OH)$_2$ NWs/RGO and β-Ni(OH)$_2$ NPs/RGO, (**d**) the fitting value of Rs and Rct resistance.

The CV plots of β-Ni(OH)$_2$ NWs/RGO electrode at different scan rates are shown in Fig. 4b. As the scan rate increases, the oxidation peak moves to the positive direction and the reduction peak moves to the negative direction, and the $E_O - E_R$ value is constantly increasing, due to the polarization of β-Ni(OH)$_2$ NWs/RGO electrode. Furthermore, β-Ni(OH)$_2$ NWs/RGO has well-defined redox peaks at a scan rate of 1–20 mV/s, indicating β-Ni(OH)$_2$ NWs/RGO has pseudocapacitive properties.

The charge-discharge performance of β-Ni(OH)$_2$ NWs/RGO at various charge-discharge rates is shown in Fig. 5a. As the charge-discharge rate increases, the discharge capacity of the electrode material decreases due to the polarization of the electrode. The discharge specific capacity is 343.2, 325 and 272.7 mAh/g, when the discharge rate is 0.2, 1 and 5C, respectively. Due to synergistic effects of β-Ni(OH)$_2$ NWs and RGO, β-Ni(OH)$_2$ NWs/RGO shows high capacity and good rate performance, which is larger than reported in some literatures (Table S1). The addition of graphene greatly improved the electrochemical performance of Ni(OH)$_2$, which is similar to the graphene-based composites reported in some literature[46–48].

Figure 5b shows the cycling stability plots of Ni(OH)$_2$/RGO electrode at various discharge rates. The average discharge capacities for α-Ni(OH)$_2$ NWs/RGO, β-Ni(OH)$_2$ NWs/RGO and β-Ni(OH)$_2$ NPs/RGO are 368, 343.5 and 288 mAh/g at the discharge rate of 0.2C, and decrease to 238.9, 272.1 and 207.9 mAh/g at the discharge rate of 5C, respectively. This is related to the fact that Ni(OH)$_2$ nanowires can provide fast transfer channels for ions and electrons compared to Ni(OH)$_2$ nanosheets. After 100 cycles, the β-Ni(OH)$_2$ NWs/RGO has almost no capacity loss at the discharge rate of 5C, suggesting that the composite has a good cycling durability. This is ascribed to the synergistic effects of β-Ni(OH)$_2$ NWs and RGO.

Figure 5c shows the resistance characteristics of the Ni(OH)$_2$/RGO electrode were investigated by EIS measurements. In the medium frequency range, the diffusion of the three electrode materials in the electrolyte is not much difference. In the inset, the intrinsic solution resistance (R_S) and the charge transfer resistances (R_{ct}) are corresponding to the intercept on the real axis and the diameter of the flat semicircle in the high frequency range, respectively[49]. In Fig. 5d, Ni(OH)$_2$/RGO electrodes with 3D network-like have smaller R_S and R_{ct} values compared

with β-Ni(OH)$_2$/RGO with nanosheets. Apparently, β-Ni(OH)$_2$ NWs/RGO composite is an ideal positive material for high performance Ni-MH batteries.

Conclusion

In summary, we have successfully prepared 3D β-Ni(OH)$_2$ NWs/RGO composite via a simple phase transformation method. In NaOH aqueous solution, Paraotwayite type α-Ni(OH)$_2$ nanowires have completely transformed into β-Ni(OH)$_2$ nanowires when the hydrothermal time was 30 min, and its morphology was still unchanged. The capacity and cycling durability of β-Ni(OH)$_2$ NWs/RGO composite was superior to α-Ni(OH)$_2$ NWs/RGO composite and β-Ni(OH)$_2$ NPs/RGO composite at high discharge rate. Owing to synergistic effects of nanowires and RGO layer, β-Ni(OH)$_2$ NWs/RGO composite exhibited high capacity performance and excellent stability.

Methods

Preparation of 3D α-Ni(OH)$_2$ NWs/RGO composite. GO was prepared by the modified Hummers method. 100 mg GO was dispersed into 60 mL of deionized water via ultrasonic bath for 2 h to form homogeneous GO suspension. NiSO$_4$·6H$_2$O aqueous solution (20 mL, 0.88 M) and NaOH aqueous solution (20 mL, 0.88 M) was slowly and sequentially dropped into GO suspension under vigorous stirring, and stirred for 10 min. The as-formed suspension was sealed into a 150 mL autoclave. After reaction 120 °C for 24 h, 3D α-Ni(OH)$_2$ NWs/RGO composite was collected by vacuum filtration, washed three times with deionized water and absolute ethanol, and then freeze-dried for 24 h.

Preparation of 3D β-Ni(OH)$_2$ NWs/RGO and β-Ni(OH)$_2$ NPs/RGO composites. 160 mg 3D α-Ni(OH)$_2$ NWs/RGO composite was dispersed into NaOH aqueous solution (80 mL, 0.025 M) with vigorous stirring for 30 min. Afterwards, the reaction solution was sealed into a 100 mL autoclave and heated to 180 °C for 30 min and 60 min to synthesis 3D β-Ni(OH)$_2$ NWs/RGO and β-Ni(OH)$_2$ NPs/RGO composites, respectively. To obtain the final product, the obtained mixture was filtrated and washed with deionized water and absolute ethanol, and then freeze-dried for 24 h.

The crystal structures of prepared samples were characterized by Bruker D8 Advance X-ray diffraction (XRD) with Cu Kα radiation ($\lambda = 0.15406$ nm); The morphologies and microstructures of prepared samples were observed by field-emission scanning electron microscope (FESEM, Carl Zeiss Sigma 500) and high-resolution transmission electron microscopy (HRTEM, FEI Tecnai G^2 F20 S-TWIN). X-ray photoelectron spectroscopy (XPS, Thermo Scientific, ESCALAB 250 XI), Infrared spectrum (IR, NICOLET 380), and Raman spectroscopy (Bruker, SENTERRA) measurements were employed to study the physical properties of the samples. The active materials, conducting acetylene black and polytetrafluoroethylene (weight ratio of 8:1:1) were added into ethanol solution. The slurry was fabricated and loaded onto the 1 * 1 cm^2 nickel foam, the working electrodes were obtained. The load mass of each electrode is approximately 2 mg/cm^2. The electrochemical data was measured by using CT2001A cell test station (LANHE, China) and CHI760E electrochemical workstation (Chenhua, China) under a three-electrode cell configuration at room temperature in 6 M KOH.

References

1. Shinyama, K. *et al*. Deterioration mechanism of nickel metal-hydride batteries for hybrid electric vehicles. *J. power sources* **141**, 193–197, https://doi.org/10.1016/j.jpowsour.2004.09.010 (2005).
2. Fang, D. L., Chen, Z. D., Liu, X., Wu, Z. F. & Zheng, C. H. Homogeneous growth of nano-sized β-Ni(OH)$_2$ on reduced graphene oxide for high-performance supercapacitors. *Electrochim. Acta* **81**, 321–329, https://doi.org/10.1016/j.electacta.2012.07.047 (2012).
3. Huang, M. *et al*. Facile synthesis of single-crystalline NiO nanosheet arrays on Ni foam for high-performance supercapacitors. *CrystEngComm* **16**, 2878, https://doi.org/10.1039/c3ce42335b (2014).
4. Le, Q. J., Wang, T., Zhu, S. J., Zhang, J. M. & Zhang, Y. X. Facile synthesis of carbon sphere@Ni(OH)$_2$ and derivatives for high-performance supercapacitors. *Funct. Mater. Lett.* 1642002, https://doi.org/10.1142/S1793604716420029 (2016).
5. Zhu, Y. F. *et al*. PPy@NiCo$_2$S$_4$ nanosheets anchored on graphite foam with bicontinuous conductive network for high-areal capacitance and high-rate electrodes. *J. Alloys Compd.* **711**, 643–651, https://doi.org/10.1016/j.jallcom.2018.02.346 (2018).
6. Wang, F. F. *et al*. Co-doped Ni$_3$S$_2$@CNT arrays anchored on graphite foam with a hierarchical conductive network for high-performance supercapacitors and hydrogen evolution electrodes. *J. Mater. Chem. A* **6**, 10490–10496, https://doi.org/10.1039/c8ta03131b (2018).
7. Guo, X. L. *et al*. Quasi-parallel arrays with a 2D-on-2D structure for electrochemical supercapacitors. *J. Mater. Chem. A* **6**, 24717–24727, https://doi.org/10.1039/c8ta07869f (2018).
8. Taniguchi, A., Fujioka, N., Ikoma, M. & Ohta, A. Development of nickel/metal-hydride batteries for EVs and HEVs. *J. power sources* **100**, 117–124, https://doi.org/10.1016/S0378-7753(01)00889-8 (2001).
9. Mi, X. *et al*. High temperature performances of yttrium-doped spherical nickel hydroxide. *Electrochim. Acta* **49**, 3361–3366, https://doi.org/10.1016/j.electacta.2004.03.005 (2004).
10. Liu, Y. F., Pan, H. G., Gao, M. X. & Wang, Q. D. Advanced hydrogen storage alloys for Ni/MH rechargeable batteries. *J. Mater. Chem.* **21**, 4743–4755, https://doi.org/10.1039/c0jm01921f (2011).
11. Wu, X. H., Feng, Q. P., Wang, M. & Huang, G. W. Spherical Al-substituted α-nickel hydroxide with high tapping density applied in Ni-MH battery. *J. Power Sources* **329**, 170–178, https://doi.org/10.1016/j.jpowsour.2016.08.072 (2016).
12. Li, B. J. *et al*. Improved performances of β-Ni(OH)$_2$@reduced-graphene-oxide in Ni-MH and Li-ion batteries. *Chem. Commun.* **47**, 3159–3161, https://doi.org/10.1039/c0cc04507a (2011).
13. Ji, J. Y. *et al*. Nanoporous Ni(OH)$_2$ thin film on 3D ultrathin-graphite foam for asymmetric supercapacitor. *Acs Nano* **7**, 6237–6243, https://doi.org/10.1021/nn4021955 (2013).
14. Xu, L. P. *et al*. 3D Flowerlike α-Nickel Hydroxide with Enhanced Electrochemical Activity Synthesized by Microwave-Assisted Hydrothermal Method. *Chem. Mater.* **20**, 308–316, https://doi.org/10.1021/cm702207w (2008).
15. Tang, Y. F. *et al*. Template-free hydrothermal synthesis of nickel cobalt hydroxide nanoflowers with high performance for asymmetric supercapacitor. *Electrochim. Acta* **161**, 279–289, https://doi.org/10.1016/j.electacta.2015.02.095 (2015).
16. Ji, W. J. *et al*. Polypyrrole encapsulation on flower-like porous NiO for advanced high-performance supercapacitors. *Chem. Commun.* **51**, 7669–7672, https://doi.org/10.1039/c5cc00965k (2015).

17. Wang, H. Z., Shi, X., Zhang, W. G. & Yao, S. W. One-pot hydrothermal synthesis of flower-like β-Ni(OH)$_2$, encapsulated by reduced graphene oxide for high-performance supercapacitors. *J. Alloys Compd.* **711**, 643–651, https://doi.org/10.1016/j.jallcom.2017.04.035 (2017).

18. Zhou, W. *et al.* Hydrazine-linked convergent self-assembly of sophisticated concave polyhedrons of β-Ni(OH)$_2$ and NiO from nanoplate building blocks. *J. Am. Chem. Soc.* **131**, 2959–2964, https://doi.org/10.1021/ja808784s (2009).

19. Fu, W. D. *et al.* β-Ni(OH)2 nanosheets grown on graphene as advanced electrochemical pseudocapacitor materials with improved rate capability and cycle performance. *Materials Letters* **134**, 107–110, https://doi.org/10.1016/j.matlet.2014.07.063 (2014).

20. Zang, X. X., Sun, C. C., Dai, Z. Y., Yang, J. & Dong, X. C. Nickel hydroxide nanosheets supported on reduced graphene oxide for high-performance supercapacitors. *J. Alloys Compd.* **691**, 144–150, https://doi.org/10.1016/j.jallcom.2016.08.233 (2017).

21. Liu, Y. *et al.* Enhanced sensitivity of a GHz surface acoustic wave humidity sensor based on Ni(SO$_4$)$_{0.3}$(OH)$_{1.4}$ nanobelts and NiO nanoparticles. *J. Mater. Chem. C* **3**, 9902–9909, https://doi.org/10.1039/c5tc02138c (2015).

22. Lai, F. L., Huang, Y. P., Miao, Y. E. & Liu, T. X. Controllable preparation of multi-dimensional hybrid materials of nickel-cobalt layered double hydroxide nanorods/nanosheets on electrospun carbon nanofibers for high-performance supercapacitors. *Electrochim. Acta* **174**, 456–463, https://doi.org/10.1016/j.electacta.2015.06.031 (2013).

23. Dong, L., Chu, Y. & Sun, W. Controllable synthesis of nickel hydroxide and porous nickel oxide nanostructures with different morphologies. *Chem. Eur. J.* **14**, 5064–5072, https://doi.org/10.1002/chem.200701627 (2008).

24. Du, H. M., Jiao, L. F., Cao, K. Z., Wang, Y. J. & Yuan, H. T. Polyol-mediated synthesis of mesoporous α-Ni(OH)$_2$ with enhanced supercapacitance. *Acs Appl. Mater. Interfaces* **5**, 6643–6648, https://doi.org/10.1021/am401341h (2013).

25. Gao, T. & Jelle, B. P. Paraotwayite-type α-Ni(OH)$_2$ nanowires: structural, optical, and electrochemical properties. *J. Phys. Chem. C* **117**, 17294–17302, https://doi.org/10.1021/jp405149d (2013).

26. Memon, J. *et al.* Synthesis of graphene/Ni–Al layered double hydroxide nanowires and their application as an electrode material for supercapacitors. *J. Mater. Chem. A* **2**, 5060–5067, https://doi.org/10.1039/c3ta14613h (2014).

27. Zhang, L. L., Xiong, Z. G. & Zhao, X. S. A composite electrode consisting of nickel hydroxide, carbon nanotubes, and reduced graphene oxide with an ultrahigh electrocapacitance. *J. Power Sources* **222**, 326–332, https://doi.org/10.1016/j.jpowsour.2012.09.016 (2013).

28. Jiang, C. H., Zhan, B. B., Li, C., Huang, W. & Dong, X. C. Synthesis of three-dimensional self-standing graphene/Ni(OH)$_2$ composites for high-performance supercapacitors. *RSC Adv.* **4**, 18080–18085, https://doi.org/10.1039/c4ra00916a (2014).

29. Yang, S. B. *et al.* Spherical α-Ni(OH)$_2$ nanoarchitecture grown on graphene as advanced electrochemical pseudocapacitor materials. *Chem. Commun.* **48**, 2773–2775, https://doi.org/10.1039/c2cc16565a (2012).

30. Bai, X. *et al.* Rational design of sandwiched Ni-Co layered double hydroxides hollow nanocages/graphene derived from metal-organic framework for sustainable energy storage. *ACS Sustainable Chem. Eng.* **5**, 9923–9934, https://doi.org/10.1021/acssuschemeng.7b01879 (2017).

31. Zhang, H. T. *et al.* One-Step Electrophoretic Deposition of Reduced Graphene Oxide and Ni(OH)$_2$ Composite Films for Controlled Syntheses Supercapacitor Electrodes. *J. Phys. Chem. B* **117**, 1616–1627, https://doi.org/10.1021/jp305198j (2013).

32. Jeevanandam, P., Koltypin, Y. & Gedanken, A. Synthesis of nanosized α-nickel hydroxide by a sonochemical method. *Nano Letters* **1**, 263–265, https://doi.org/10.1021/nl010003p (2001).

33. Bastakoti, B. P., Huang, H. S., Chen, L. C., Wu, K. C. & Yamauchi, Y. Block copolymer assisted synthesis of porous α-Ni(OH)$_2$ microflowers with high surface areas as electrochemical pseudocapacitor materials. *Chem. Commun.* **48**, 9150–9152, https://doi.org/10.1039/c2cc32945j (2012).

34. Liu, W. *et al.* Ionic liquid-assisted grown of beta-nickel hydroxide nanowires on reduced graphene oxide for high-performance supercapacitors. *Electrochim. Acta* **143**, 135–142, https://doi.org/10.1016/j.electacta.2014.08.010 (2014).

35. Ma, X. W., Liu, J. W., Liang, C. Y., Gong, X. W. & Che, R. C. A facile phase transformation method for the preparation of 3D flower-like β-Ni(OH)$_2$/GO/CNTs composite with excellent supercapacitor performance. *J. Mater. Chem. A* **2**, 12692–12696, https://doi.org/10.1039/c4ta02221a (2014).

36. Zhu, J. X. *et al.* Facile synthesis of metal oxide/reduced graphene oxide hybrids with high lithium storage capacity and stable cyclability. *Nanoscale* **3**, 1084–1089, https://doi.org/10.1039/c0nr00744g (2011).

37. Li, Z., Han, J., Fan, L. & Guo, R. *In-situ* controllable growth of α-Ni(OH)$_2$, with different morphologies on reduced graphene oxide sheets and capacitive performance for supercapacitors. *Colloid Polym Sci.* **294**, 681–689, https://doi.org/10.1007/s00396-015-3826-y (2016).

38. Zhuo, M. *et al.* High-performance humidity sensors from Ni(SO$_4$)$_{0.3}$(OH)$_{1.4}$ nanobelts. *Nanoscale* **6**, 6521–6525, https://doi.org/10.1039/c4nr00277f (2014).

39. Xu, Y. X. *et al.* One-step strategy to graphene/Ni(OH)$_2$, composite hydrogels as advanced three-dimensional supercapacitor electrode materials. *Nano Res.* **6**, 65–76, https://doi.org/10.1007/s12274-012-0284-4 (2013).

40. Abbas, S. A., Iqbal, M. I., Kim, S. H., Khan, H. A. & Jung, K. D. Facile synthesis of alfa-nickel hydroxide by an ultrasound-assisted method and its application in energy storage devices. *Appl. Surf. Sci.* **474**, 218–226, https://doi.org/10.1016/j.apsusc.2018.03.036 (2019).

41. Schedin, F. *et al.* Surface-enhanced raman spectroscopy of graphene. *Acs Nano* **4**, 5617–5626, https://doi.org/10.1021/nn1010842 (2010).

42. Cai, X. Q. *et al.* Solvothermal synthesis of NiCo-layered double hydroxide nanosheets decorated on RGO sheets for high performance supercapacitor. *Chem. Eng. J.* **268**, 251–259, https://doi.org/10.1016/j.cej.2015.01.072 (2015).

43. Min, S. D., Zhao, C. J., Chen, G. R. & Qian, X. Z. One-pot hydrothermal synthesis of reduced graphene oxide/Ni(OH)$_2$ films on nickel foam for high performance supercapacitors. *Electrochim. Acta* **115**, 155–164, https://doi.org/10.1016/j.electacta.2013.10.140 (2014).

44. Nagaraju, G., Cha, S. M. & Yu, J. S. Ultrathin nickel hydroxide nanosheet arrays grafted biomass-derived honeycomb-like porous carbon with improved electrochemical performance as a supercapacitive material. *Sci. Rep.* **7**, 45201, https://doi.org/10.1038/srep45201 (2017).

45. Wang, H. Z., Shi, X., Zhang, W. G. & Yao, S. W. One-pot hydrothermal synthesis of flower-like β-Ni(OH)$_2$ encapsulated by reduced graphene oxide for high-performance supercapacitors. *J. Alloys Compd.* **711**, 643–651, https://doi.org/10.1016/j.jallcom.2017.04.035 (2017).

46. Ji, J. Y. *et al. In Situ* Activation of Nitrogen-Doped Graphene Anchored on Graphite Foam for a High Capacity Anode. *ACS Nano* **9**, 8609–8616, https://doi.org/10.1021/acsnano.5b03888 (2015).

47. Zhu, Y. F. *et al.* Liquid-Solid-Solution Assembly of CoFe$_2$O$_4$/Graphene Nanocomposite as a High-Performance Lithium-Ion Battery Anode. *Electrochim. Acta* **215**, 247–252, https://doi.org/10.1016/j.electacta.2016.08.057 (2016).

48. Cui, X. H. *et al.* Enhanced rate capability of a lithium ion battery anode based on liquid–solid-solution assembly of Fe$_2$O$_3$ on crumpled graphene. *RSC Adv.* **6**, 9007–9012, https://doi.org/10.1039/C5RA22408J (2016).

49. Dong, S. *et al.* One-step electrochemical synthesis of three-dimensional graphene foam loaded nickel-cobalt hydroxides nanoflakes and its electrochemical properties. *Electrochim. Acta* **152**, 195–201, https://doi.org/10.1016/j.electacta.2014.09.061 (2015).

Acknowledgements

Author Contributions

Additional Information

Supplementary information accompanies this paper at https://doi.org/10.1038/s41598-019-47120-9.

Competing Interests: The authors declare no competing interests.

Publisher's note: Springer Nature remains neutral with regard to jurisdictional claims in published maps and institutional affiliations.